VOL. 26, NO. 12, DECEMBER 1989 J. AIRCRAFT

Rotor Hover Performance Prediction Using a Free-Wake, Computational Fluid Dynamics Method

K. Ramachandran*
Flow Analysis, Inc., Mountain View, California
and
C. Tung† and F. X. Caradonna‡
NASA Ames Research Center, Moffett Field, California

A method for predicting rotor hover performance is described. This method solves the compressible mass conservation equation much like current full-potential codes and therefore can predict transonic flows on a rotor. The newly developed approach also allows for the free convection of shed vorticity and permits the computation of the entire hover wake system. The method uses a vortex embedding scheme in potential flow and has been implemented in a computer code, HELIX I. A simple boundary layer and two different induced-drag integration schemes are included for power predictions. The induced drag is obtained from surface pressure integration and an energy flux integral. Comparisons between computations and experiment show good agreement for the prediction of power polars, surface pressure distribution, and tip vortex geometry.

Introduction

THE performance of helicopter rotors is dominated by the strength, structure, and location of the shed wake (Fig. 1). Our inability to predict these wakes is a very old problem and a primary impediment to the accurate prediction of hover performance. All previous hover free-wake prediction methods employ integral formulations of the flow problem and most fail to accurately predict the convection of the shed tip vortex. Lacking this quantity, we cannot predict the distance between a blade and the nearest tip vortex from a previous blade. Therefore, one typically does not obtain an accurate induced velocity and power.

Most current methods for computing rotor flowfields can be classified under two broad categories: 1) integral methods in the form of lifting line or lifting surface method[1-3] and 2) finite difference[4-6] methods based on potential, Euler, or Navier-Stokes solvers. Finite-difference methods are generally too dissipative to predict a full hover wake with a realistic grid. Therefore, these methods are typically coupled[7,8] to an integral method which then predicts the wake and its induced inflow. In this paper, an alternative finite-volume scheme[9] is described that uses a vortex embedding procedure which allows us to put vorticity layers anywhere in the grid.

Solution Method

The potential flow equation, which expresses conservation of mass for compressible irrotational flow, is given by

$$\nabla \cdot (\rho V) = 0 \tag{1}$$

with the isentropic relation for density

$$\rho = \left\{1 - \left(\frac{\gamma-1}{2}\right) M_\infty^2 \left[(\omega \times r)^2 - q^2\right]\right\}^{\frac{1}{\gamma-1}} \tag{2}$$

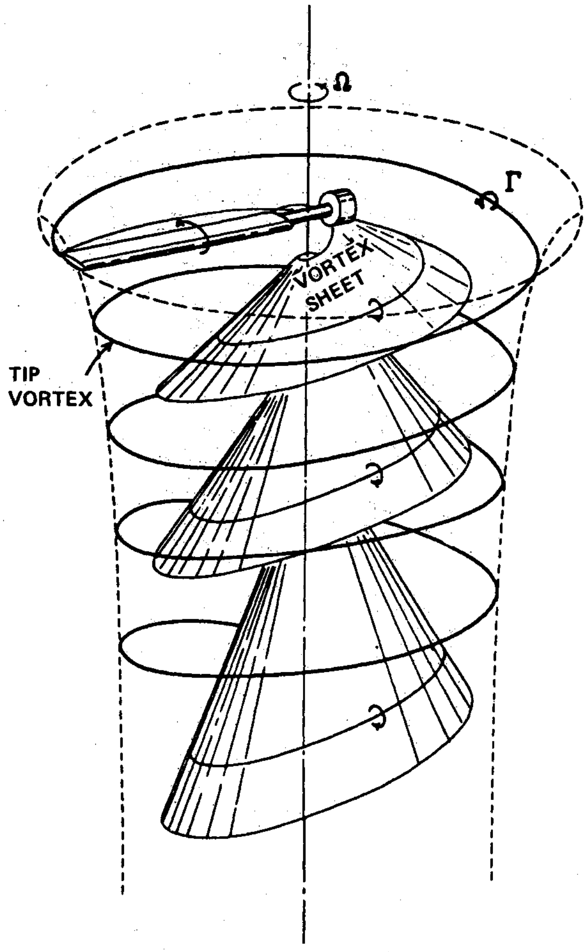

Fig. 1 Schematic of rotor wake structure (from Ref. 1).

Presented as Paper 89-0638 at the AIAA 27th Aerospace Sciences Meeting, Reno, NV, Jan. 9-12, 1989; received Jan. 23, 1989; revision received May 30, 1989.

*Research Scientist. Member AIAA.

†Research Scientist, Aeroflightdynamics Directorate, U.S. Army Aviation Research and Technology Activity (AVSCOM).

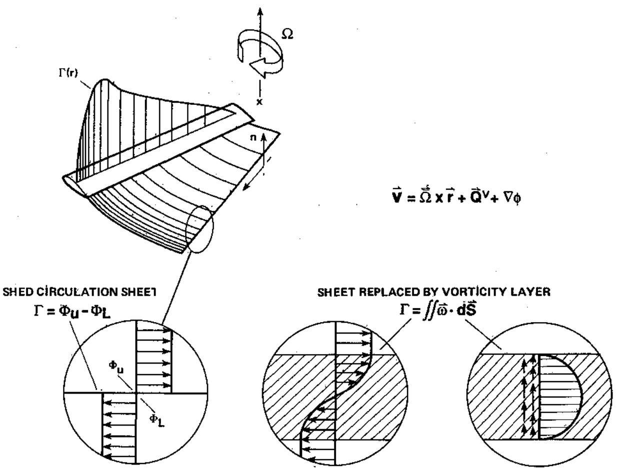

Fig. 2 Alternate models of the shed wake.

where

$$V = \Omega \times r + \nabla \Phi \tag{3}$$

This flow model has a basic flaw when the shed circulation sheet is a fundamental part of the problem. With a potential alone, this sheet can only be represented by a surface along which Φ is discontinuous and where the magnitude of this discontinuity, Γ, is the shed circulation. This sheet requires special coding logic which constrains it to lie along a grid coordinate. This constraint can be eliminated by redefining V as

$$V = \Omega \times r + \nabla \phi + q^v \tag{4}$$

That is, the flow is decomposed into irrotational ($\nabla\phi$) and rotational (q^v) fields defined for the entire solution domain. (Note: $\Omega \times r$ results from a rotational coordinate transformation and has no fundamental effect on the flow kinematics.) In this description, the shed circulation can be described as a thin region of vorticity, $\omega = \nabla \times q^v$, and ϕ is continuous. The essential simplification results because the use of q^v does not effect the physical validity of Eq. (1) and has only a minor effect on its coding. The vortical velocity, q^v does violate the irrotational assumption which underlies Eq. (2). However, q^v is nonzero only in regions whose small size (i.e., thinness) results in no significant effect on the flow. With this modification, our coding is not grid dependent and we are free to convect q^v.

This decomposition is made especially powerful by the fact that for a given ω distribution, q^v is not unique and can be imposed in several ways. The intuitive urge is to impose q^v as a tangential field (Fig. 2). However, such a q^v must be nonzero throughout the entire solution domain and is very costly to compute.

A computationally efficient representation of q^v is that of a distribution of spread velocity normal to the vortex sheet. This representation seems very unphysical until one considers that this is not the entire velocity which is represented, but merely the vortical portion q^v. The distribution of total velocity V must actually have a tangential form after the potential portion $\nabla\phi$ is added. The vortical part q^v can have any form as long as $\omega = \nabla \times q^v$. The normal form of q^v has the advantage of being nonzero only in a thin region, just like ω.

To find the required strength of q^v, we use Gauss' theorem to obtain a relation from the integral of q^v along a normal through each point on the sheet:

$$\Gamma = \iint \frac{\partial q^v}{\partial s} \, ds \, dn \tag{5}$$

The circulation Γ is known at the upstream edge of the sheet (blade trailing edge) from the lift distribution (which is computed as part of the entire calculation). Since Γ is constant along mean streamlines within the sheet, it can easily be computed on the entire sheet. This Γ distribution provides a scaling factor which gives the magnitude of q^v as soon as the width and the functional form of q^v are determined. This width and functional form can be found using a viscous solution or by simply choosing computationally convenient values. For the hover wake problem, the later approach suffices. A particularly simple and accurate form for q^v involves a Clebsch-type[10] of representation:

$$q^v = \Gamma^c \nabla \Psi \tag{6}$$

where $\Gamma^c(r)$ is a three-dimensional field which smoothly goes to the appropriate Γ (circulation value) on the sheet as r approaches the sheet surface. A convenient formula for $\Psi(r)$ is

$$\Psi(r) = \tfrac{1}{2}\sin(\pi S_n/2a), \qquad |S_n| \leq a/2 \tag{7a}$$

$$\Psi(r) = +\tfrac{1}{2}, \qquad S_n > +a/2 \tag{7b}$$

$$\Psi(r) = -\tfrac{1}{2}, \qquad S_n < -a/2 \tag{7c}$$

where S_n is a (signed) normal distance from the point r to the sheet. The Clebsch's potential $\Psi(r)$ smoothly goes from $+0.5$ on one side of the sheet to -0.5 on the other. We use interpolation-like formulas to compute $\Gamma^c(r)$ and $S_n(r)$ at any grid point r:

$$\Gamma_c(r) = \left[\sum_\ell \Gamma_\ell \sigma(\Delta r_\ell)\right] \Big/ A \tag{8}$$

$$S_n(r) = \left[\sum_\ell S_\ell^n(r, r_\ell)\sigma(\Delta r_\ell)\right] \Big/ A \tag{9}$$

where

$$A = \sum_\ell \sigma(\Delta r_\ell)$$

$$\Delta r_\ell = |r - r_\ell|$$

and the Γ_l is the circulation defined for each marker l that defines the sheet. It remains constant on each marker from the point on the blade trailing edge where it is shed. Also, $S_\ell^n(r, r_\ell)$ is the normal distance from r to a plane tangent to the sheet at marker l, and the spreading function $\sigma(\Delta r_\ell)$ is

$$\sigma(\Delta r_\ell) = \max(0, 1 - \Delta r_\ell / a^2) \tag{10}$$

where a is a specified spreading distance, which is some convenient function of local grid size.

Even though Ψ is nonzero throughout the field (except on the sheet), $\nabla\Psi$ is zero beyond the spreading distance from the sheet. Accordingly, both $\Gamma^c(r)$ and $\Psi(r)$ need be computed only on those grid points that are in a narrow band about the sheet with thickness of the order of the spreading distance.

The major computational work is the solution of Eq. (1) for $\phi(r, \psi, z)$, where r, ψ, z represent radial, azimuthal, and axial coordinates, respectively. A blade fixed H-grid is used to solve for the potential. In the azimuthal direction, all flow quantities are taken to be periodic with period $2\pi/N$, where N is the number of blades. During each iteration, a rapidly converging approximate factorization scheme is used to solve Eq. (1) with q^v fixed. This procedure is described in detail in Ref. 9. The resulting solution process is an iteration between solving the mass equation and convecting the shed vorticity. A four-step procedure is repeatedly used:

1) The vortex sheet position is integrated as a set of marker streamlines which follow the flow using interpolated values of V from the fixed grid.

2) q^v is computed at grid points near the sheet.

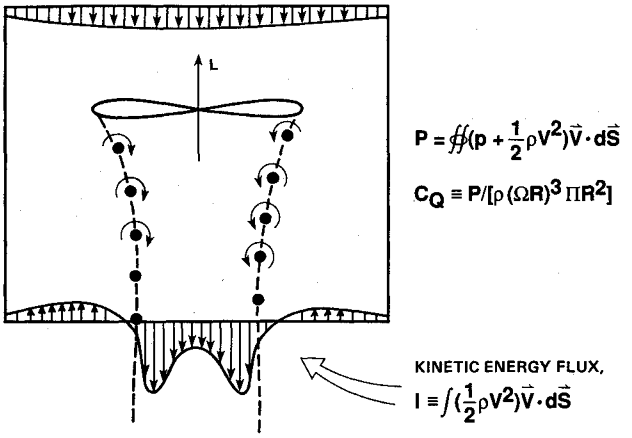

Fig. 3 Induced power by energy-flux integration.

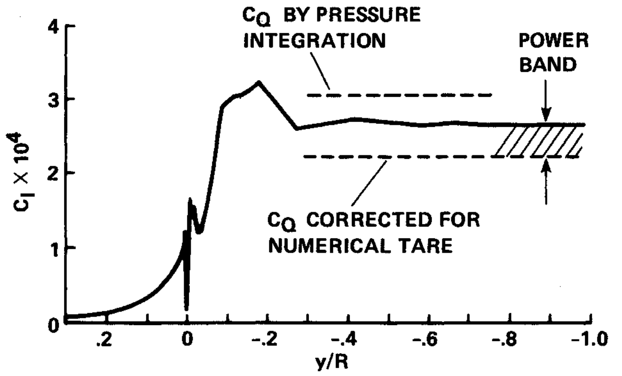

Fig. 4 Comparison of surface pressure integration and kinetic energy-flux integration to find power. [Landgrebe hover model, 4 blades, twist = −8 deg, $\Theta_{0.75}$ = 6 deg, aspect ratio = 13.6, and NACA 0012 (same rotor as for Figs. 10–13)].

3) A potential ϕ is computed at all grid points by solving the compressible mass conservation equation using a modified finite-volume potential flow technique.

4) A new velocity V is computed at each grid point after adding q^v to the potential and freestream components of the velocity. At convergence the vortex sheet follows the flow.

This procedure is implemented in the code HELIX I.

Drag Mechanisms

The major task in helicopter rotor performance analysis is the calculation of the rotor lift and power. Typically, lift is found by surface pressure integration and is well predicted by finite-difference methods when the induced inflow is well modeled. This is usually reflected in good comparisons of blade surface pressures with measured data.[5] However, power depends on drag which is a much smaller force than lift and is very sensitive to small changes (and errors) in surface pressure. Nevertheless, surface pressure integration is simple and is usually the first means used to compute drag. Such integrations typically produce a spurious numerical drag which is a function of the grid and the flow. The usual way of treating this is to subtract it as a tare from the pressure integrations. The value of the tare is found by performing nonlifting subcritical three-dimensional computations and lifting, subcritical, and two-dimensional computations. We find a tare drag coefficient of 0.0075 to be typical for a NACA 0012 airfoil. This value is independent of Mach number (for subcritical flows) and slightly dependent on lift, being a maximum at zero lift. We employ this tare for all of the shown pressure integrations for drag.

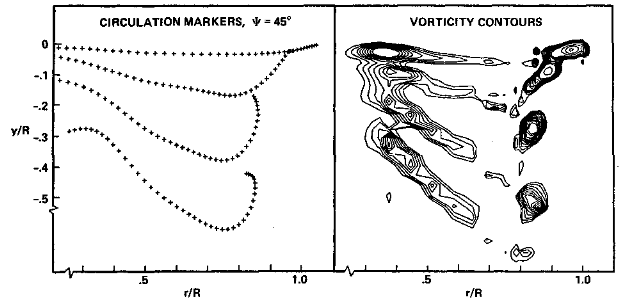

Fig. 5 Computed wake structure for the BHC 360 rotor (tapered tip, nonconstant twist, $\Theta_{0.75} = 6.87$, and $C_T = 0.007$).

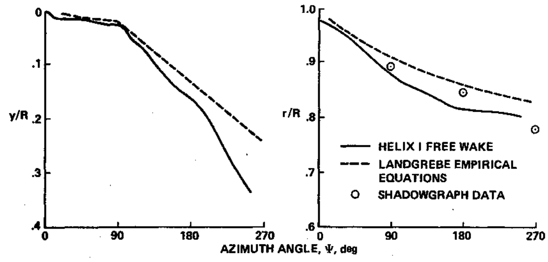

Fig. 6 Axial and radial tip vortex convection for the BHC 360 rotor.

Induced drag is the predominant hover drag mechanism and can account for nearly 75% of the total power. The importance of this term requires a means other than the previously mentioned pressure integral to find induced power. A convenient approach is to find power by integrating the total energy flux across the surface of a control volume containing the rotor,

$$P = \iint (p + \tfrac{1}{2}\rho V^2) V \cdot dS \tag{11}$$

$$C_Q \equiv \frac{P}{\rho(\Omega R)^3(\pi R^2)} \tag{12}$$

where C_Q is the power coefficient (Fig. 3). The major contribution to the energy flux integral comes from the downstream boundary, where the rotor wake passes through. Furthermore, in the downstream boundary it is found that the contribution of the pressure p to the flux integral in Eq. (11) is very small. Figure 4 plots the nondimensional kinetic energy flux through a plane parallel to the rotor,

$$I = \iint (\tfrac{1}{2}\rho V^2) V \cdot dS \tag{13}$$

$$C_I \equiv \frac{I}{\rho(\Omega R)^3(\pi R^2)} \tag{14}$$

as a function of axial position with respect to the rotor. It is seen that C_I is nearly zero at $0.3R$ above the rotor and a constant beyond $0.3R$ below the rotor. The variation in C_I seen between $+0.3R$ and $-0.3R$ represents the energy exchange between the pressure and kinetic energy as well as the rotor wake contraction. Below $-0.3R$, the wake is fully contracted and C_I approaches the induced-power coefficient C_{Q_i}. Also shown in this plot are the values of C_{Q_i} obtained by pressure integration and pressure integration minus the drag tare. The range from this latter value to the energy-flux value provides a numerical induced power range.

The profile drag is the next significant power sink. Following Ref. 11, we have implemented a Nash-Macdonald integral boundary-layer module to account for weak viscous-inviscid interaction effects and to allow for an approximate determination of the skin-friction drag. In this method,[12] von Kármán's integral equation is solved for the momentum thickness θ. At each spanwise station, the appropriate two-dimensional flow quantities are determined. The Mach number distribution is the main input to the boundary-layer calculation, and is obtained on each spanwise station. The boundary-layer module can run interactively. Once the displacement thickness is obtained, its influence on the inviscid computaion can be introduced using a transpiration-velocity technique.

Results

In this section, we shall show various comparisons of computations with experiments. The intent of these cases will be to show the ability of the HELIX code to predict the wake structure, high-speed loading, profile drag, and finally the entire lift/power curve.

The resolution requirements of a computation increase with the number of blades because this decreases the spacing between the various wake elements. Figures 5 and 6 show wake computations for the Boeing 360 rotor, a four-bladed rotor with a 3:1 tip taper.[13] Figure 5 shows the structure of the computed wake in the form of circulation markers and vorticity contours at an azimuth of 45 deg behind the blade. The distinction between the tip vortex and inboard wake sheets that are the basis of all empirical wake models is clear. The tight definition of the tip vortices seen here is not practically possible with present pure finite-difference methods due to numerical dissipation. In fact, this resolution was not even possible with HELIX I until the adoption of the Clebsch potential description of the vorticity. A plot of the axial and radial location of the tip vortex as a function of time is seen in Fig. 6. Here we clearly see two distinct rates of vortex convection in the axial location. The first rate (known as K_1 in the literature) is particularly important to accurate performance prediction and HELIX I has been unique in predicting this accurately. Also included in this figure is the empirically fitted wake geometry from Ref. 1 for a blade with the same thrust coefficient, a similar twist, and a rectangular planform. It can be seen that the 360 tip vortex convects radially at a faster rate than that for the rectangular planform. Also included in this figure are several unpublished shadowgraph measurements of the vortex radial location. In general, these values fall between the 360 computation and empirical curve. The differences in the contraction that are seen here are significant and can greatly affect the tip loading. Unfortunately, such loading information is not presently available for this rotor.

Rotor data containing both loading and wake information are rare. One of the few such cases is for a two-bladed, rectangular, untwisted rotor of low aspect ratio and a NACA 0012 profile.[14] Figure 7 shows a comparison of the computed and

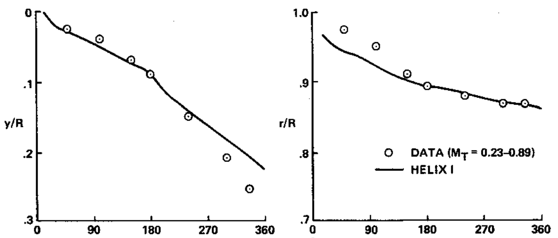

Fig. 7 Axial and radial convection of tip vortex (2-bladed hovering rotor, rectangular, untwisted, NACA 0012, aspect ratio = 6.0, and $\Theta_{0.75} = 8$ deg).

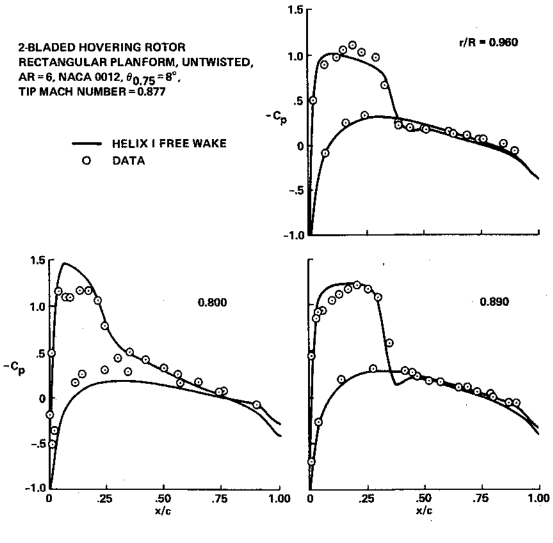

Fig. 8 Computed and measured loading on a rotor (same blade as Fig. 7; tip Mach number = 0.877).

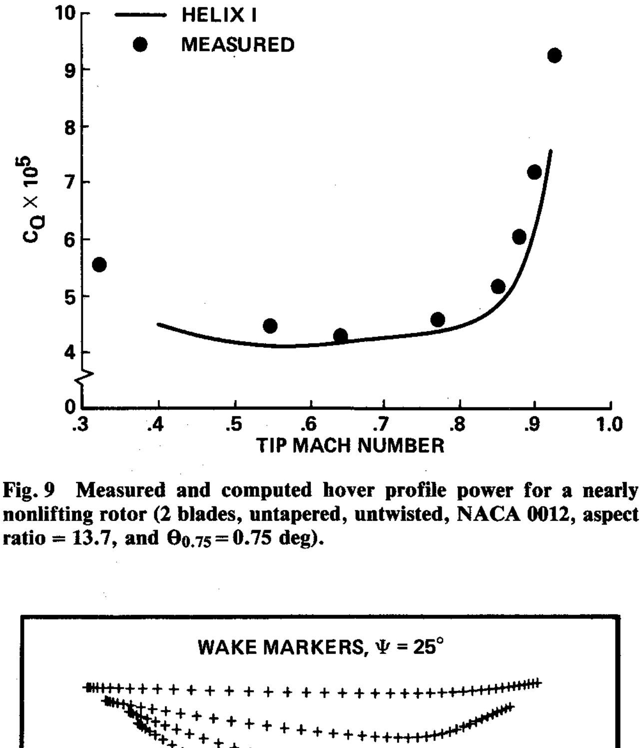

Fig. 9 Measured and computed hover profile power for a nearly nonlifting rotor (2 blades, untapered, untwisted, NACA 0012, aspect ratio = 13.7, and $\Theta_{0.75} = 0.75$ deg).

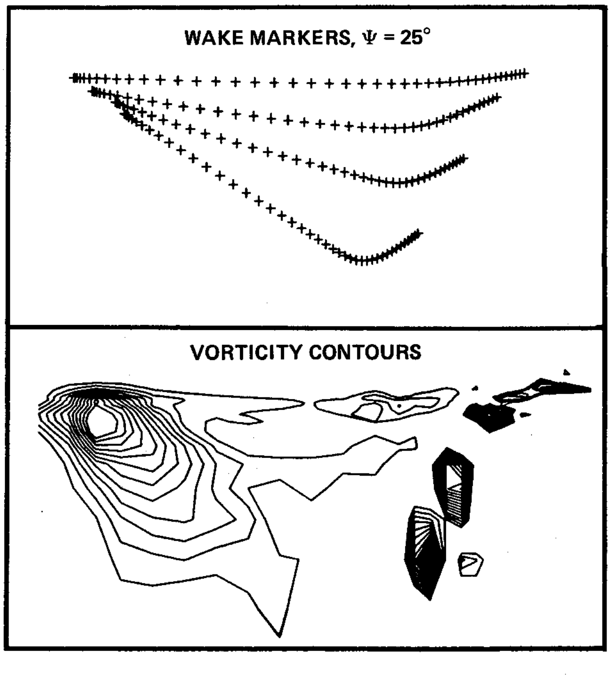

Fig. 10 Computed wake structure for a hovering rotor. (Landgrebe model rotor, 4 blades, untapered, twist = −8 deg, aspect ratio = 13.6, NACA 0012, and $\Theta_{0.75} = 8$ deg).

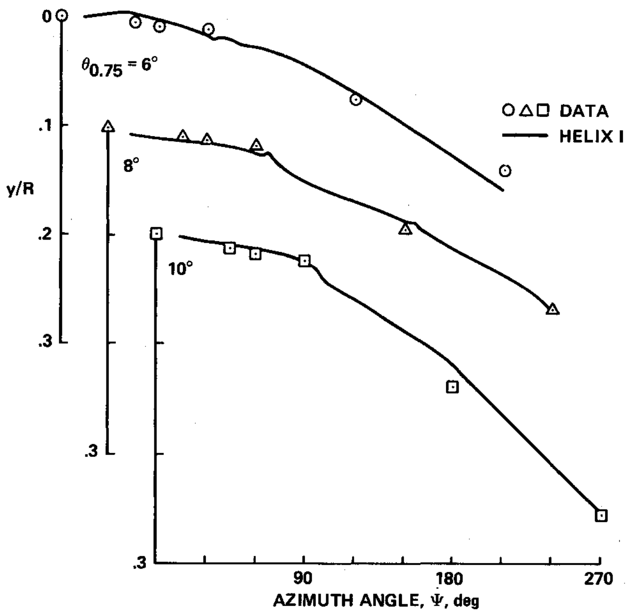

Fig. 11 Axial convection of a tip vortex (Landgrebe model rotor).

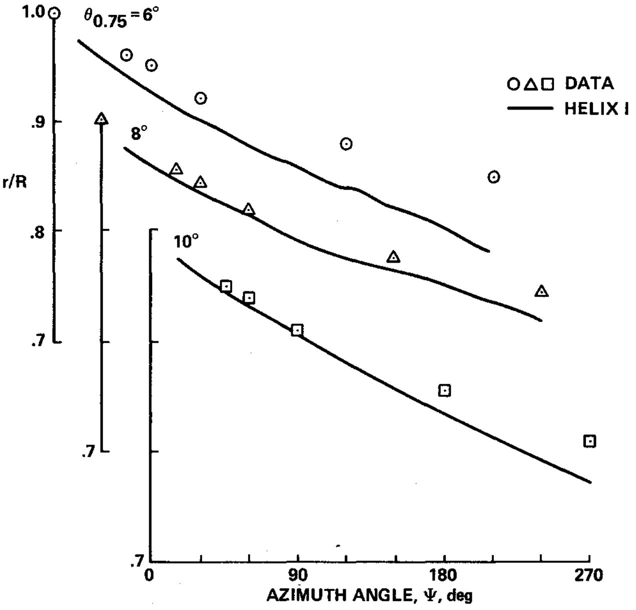

Fig. 12 Radial convection of a tip vortex (Landgrebe model rotor).

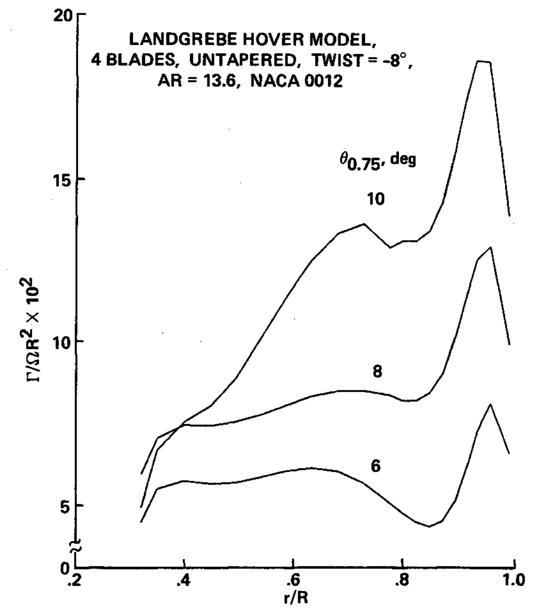

Fig. 13 Computed radial circulation distributions (Landgrebe model rotor).

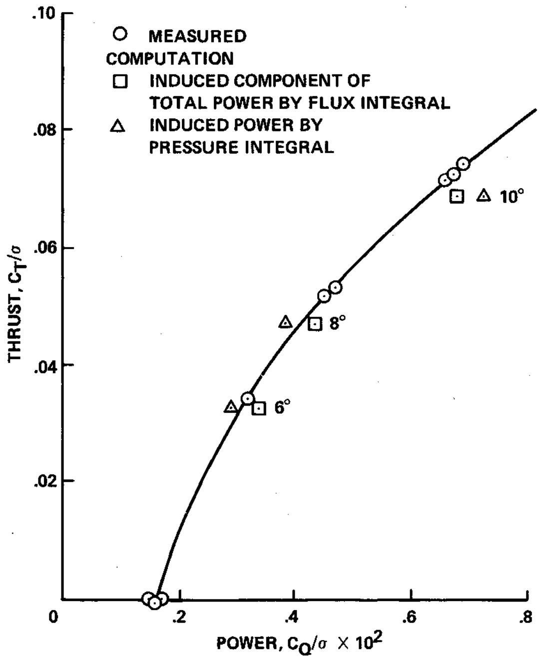

Fig. 14 Computed and measured rotor hover performance (Landgrebe model rotor).

measured axial and radial convection of the tip vortex. Again, the initial axial convection rate K_1 is very well predicted. The subsequent axial rate K_2 is underpredicted. However, K_1 is the most important of the two parameters because it determines the vortex distance of closest aproach to the blade. The radial contraction is initially overpredicted, but it rapidly converges to the experimental value for $\psi = 180$ deg and all subsequent azimuths. Thus, the free-wake prediction correctly gives the relative position of the first vortex passage with respect to the blade. Figure 8 shows the resulting predicted and measured loading in the form of chordwise pressure distributions. This case is highly transonic ($M_T = 0.877$) and it is seen that the measured shocks are well predicted. The leading-edge overexpansion and the slight trailing-edge pressure jump are probably due to the use of an artificial density (for supercritical stability) together with a grid which is optimized for the wake prediction. The point, however, is that a free wake and transonic solution can be handled by a unified analysis. Certainly, this particular computation would require a surface grid refinement if a drag computation were to be performed. Unfortunately, power is not included in the experimental data.

As a first step in demonstrating the ability to predict power, comparisons were made with experimental data for a nonlifting rotor. Suitable experimental data for such a comparison has recently been obtained in a model hover facility.[11] High-speed torque data has been obtained for a model rotor with an untapered, untwisted rectangular planform using a NACA 0012 profile. Computations of the power consumption of this model were determined by means of the previously discussed integration and the tare subtraction. In this process, the tare is assumed to be independent of Mach number. In addition to this pressure drag, we also included the integration of skin friction which is calculated from the boundary-layer module run in a noninteracting mode. Figure 9 is a plot of the measured power coefficient C_Q as a function of rotor tip Mach number. Also included in this figure are the drag computations obtained from HELIX I. The power variation is well predicted especially in the range $M_T = 0.6$–0.8. The differences seen at lower speeds can be due to the boundary layer being laminar and not well predicted by the present turbulent boundary-layer module. The transonic drag divergence is fairly well predicted, with the computed rise being at a slightly higher tip Mach number than the data indicates. This level of accuracy is more than adequate for hover purposes, where induced power constitutes the major loss.

Finally, wake predictions and total power are compared. Data suitable for this purpose were obtained by Landgrebe.[1] A four-bladed rotor with -8 deg linear twist and a rectangular planform was chosen for comparison. Computations were performed for three different collective pitch angles $\theta_{0.75}$ (defined as the pitch at $r/R = 0.75$). Figure 10 shows a typical view of the wake structure ($\theta_{0.75} = 8$ deg) as visualized by the circulation markers and vorticity contours. The axial and radial convection of the tip vortex for collective pitch angles of 6, 8, and 10 deg is shown in Figs. 11 and 12. For this rotor the prediction of K_1 and K_2 are uniformly excellent. (Note that the data symbols shown are obtained from Landgrebe empirical formulas.)

In Fig. 12, the tip vortex radial contraction is plotted as a function of azimuth. Good comparison is seen for the vortex location up to the first passage ($\psi = 90$ deg) for the 8- and 10-deg cases. The computed vortex for the 6-deg case is inboard compared to the experimental location. Figure 13 shows the spanwise blade-bound circulation distribution. It is seen that for all three cases the tip vortex induces a large circulation peak at the tip. This peak is greatest for $\theta_{0.75} = 10$ deg. This indicates that the growth of the tip vortex strength (as pitch increases) is a more important factor than the increasing axial convection.

The computed performance power polar is shown in Fig. 14 and compared to the experimental data. The two values of computed torque coefficient are corresponding to the use of surface pressure integration and total energy-flux integral for the induced component. It is seen that the comparison of thrust/power for $\theta_{0.75} = 6$ and 8 deg is excellent. At 10 deg, the power is somewhat overpredicted for presently unknown reasons. These computations used the actual experimental values for pitch. Most other codes require a pitch correction (2 deg is not uncommon) in order to match the experimental lift. Therefore, a slight underprediction of lift in these computations constitutes unusually good agreement—and probably results from the present wake modeling. This constitutes (to our knowledge) the first complete computational fluid dynamics (in the usual finite-difference/finite-volume sense) computation of rotor performance.

Concluding Remarks

The present vortex embedding method eliminates the problem of numerical vorticity diffusion and in the process produces excellent free-wake results. The code can also predict the three-dimensional transonic flow on the rotor blade. Therefore, the user is free to analyze rotors of arbitrary geometry. This contrasts with the present state-of-the-art which is typically a lifting-line analysis.

The present code can perform complete performance computations. The integral boundary-layer module that is implemented is suitable for many applications in predicting profile power. The induced power is computed both by surface pressure integration and by an energy-flux integral over a control volume. The two methods are in reasonable agreement and provide a small probable error range.

Although the HELIX code requires further validation studies and improvements, it probably constitutes an excellent design tool in its present form.

Acknowledgments

We wish to acknowledge the assistance and many useful suggestions of Roger Strawn, John Bridgeman, and Sue Fan Shyi.

References

[1] Landgrebe, A. J., "An Analytical and Experimental Investigation of Helicopter Rotor Hover Performance and Wake Geometry Characteristics," U.S. Army Air Mobility Research and Development Laboratories, Moffett Field, CA, USAAMRDL TR-71-24, June 1971.

[2] Kocurek, J. D. and Tangler, J. L., "A Prescribed Wake Lifting Surface Hover Performance Analysis," *Journal of the American Helicopter Society,* Vol. 22, Jan. 1977, pp. 24–35.

[3] Felker, F. F., Quackenbush, T. R., Bliss, D. R., and Light, J. S., "Comparisons of Predicted and Measured Rotor Performance in Hover Using a New Free-Wake Analysis," The 44th Annual Forum of the American Helicopter Society, Washington, DC, June 16–18, 1988.

[4] Caradonna, F. X., Desopper, A., and Tung, C., "Finite-Difference Modeling of Rotor Flows Including Wake Effects," The 8th European Rotorcraft Forum, Aix-en-Provence, France, Paper 2.7, Aug. 1982.

[5] Strawn, R. C. and Caradonna, F. X., "Conservative Full-Potential Model for Unsteady Transonic Rotor Flows," *AIAA Journal,* Vol. 25, Feb. 1987, pp. 193–198.

[6] Chen, C. L. and McCroskey, W. J., "Numerical Simulation of Helicopter Multibladed Rotor Flow," AIAA Paper 88-0046, Jan. 1988.

[7] Egolf, T. A. and Sparks, S. P., "Hovering Rotor Airload Prediction Using a Full-Potential Analysis with Realistic Wake Geometry," The Annual National Forum of American Helicopter Society, May 1985.

[8] Chang, I. C. and Tung, C., "Numerical Solution of the Full-Potential Equation for Rotors and Oblique Wings Using a New Wake Model," AIAA Paper 85-0268, Jan. 1985.

[9] Ramachandran, K., "Free-Wake Analysis of Helicopter Rotor Blades in Hover Using a Finite-Volume Technique," Ph.D. Thesis, Univ. of Tennessee, Knoxville, TN, Dec. 1987.

[10] Steinhoff, J. and Ramachandran, K., "A Vortex Embedding Method for Free-Wake Analysis of Helicopter Rotor Blades in Hover," 13th European Rotorcraft Forum, Arles, France, Paper 2-11, Sept. 1987.

[11] Bridgeman, J. O., Strawn, R. C., and Caradonna, F. X., "An Entropy and Viscosity Corrected Potential Method for Rotor Performance Prediction," The 44th Annual Forum of the American Helicopter Society, Washington, DC, June 16–18, 1988.

[12] Nash, J. F. and Macdonald, A. G. J., "The Calculation of Momentum Thickness in a Turbulent Boundary Layer at Mach Numbers up to Unity," Aeronautical Research Council, London, CP-963, 1967.

[13] Cowan, J., Dadone, L., and Gangwani, S., "Wind-Tunnel Test of a Pressure-Instrumented Model Scale Advanced Rotor," The 42nd Annual Forum of the American Helicopter Society, Washington, DC, June 1986.

[14] Caradonna, F. X. and Tung, C., "Experimental and Analytical Studies of a Model Helicopter Rotor in Hover," NASA TM-81232, 1981.